AD-A145 572 THE PROPAGATION AND GROWTH OF WHISTLER MODE WAVES GENERATED BY ELECTRON B..(U) IOWA UNIV IOWA CITY DEPT OF PHYSICS AND ASTRONOMY R L TOKAR ET AL. APR 84 1/1

UNCLASSIFIED U. OF IOWA-84-12 N00014-76-C-0016 F/G 4/1 NL

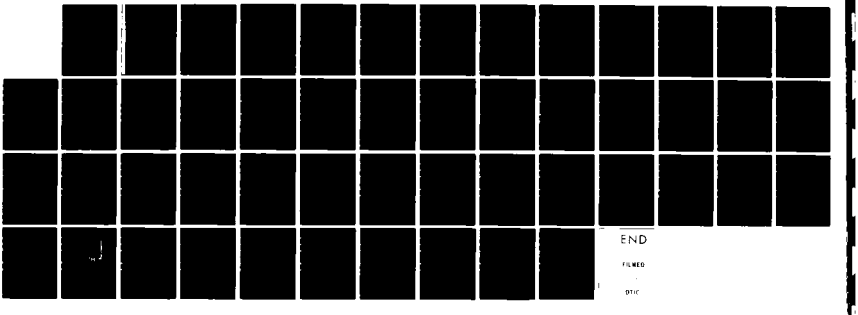

END

FILMED

DTIC

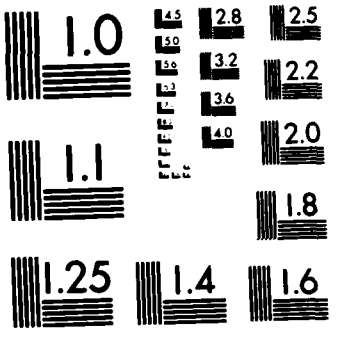

MICROCOPY RESOLUTION TEST CHART
NATIONAL BUREAU OF STANDARDS-1963-A

U. of Iowa 84-12

AD-A145 572

THE PROPAGATION AND GROWTH OF WHISTLER MODE WAVES GENERATED BY ELECTRON BEAMS IN EARTH'S BOW SHOCK

by

Robert L. Tokar* and Donald A. Gurnett

DTIC FILE COPY

SEP 1 7 1984

Department of Physics and Astronomy

THE UNIVERSITY OF IOWA

Iowa City, Iowa 52242

84 09 13 027

U. of Iowa 84-12

THE PROPAGATION AND GROWTH OF WHISTLER MODE WAVES GENERATED BY ELECTRON BEAMS IN EARTH'S BOW SHOCK

by

Robert L. Tokar* and Donald A. Gurnett

Dept. of Physics and Astronomy
The University of Iowa
Iowa City, IA 52242

*Now at Earth and Space Science Division, Los Alamos National Laboratory, Los Alamos, NM 87545

SEP 1 7 1984

This research was supported by NASA through Grant NGL-16-001-043 with NASA Headquarters and Contract NAS5-26819 with Goddard Space Flight Center and by the Office of Naval Research through Contract N00014-76-C-0016.

UNCLASSIFIED

SECURITY CLASSIFICATION OF THIS PAGE (When Data Entered)

REPORT DOCUMENTATION PAGE		READ INSTRUCTIONS BEFORE COMPLETING FORM
1. REPORT NUMBER U. of Iowa Number 84-12	2. GOVT ACCESSION NO. AD-A145522	3. RECIPIENT'S CATALOG NUMBER
4. TITLE (and Subtitle) THE PROPAGATION AND GROWTH OF WHISTLER MODE WAVES GENERATED BY ELECTRON BEAMS IN EARTH'S BOW SHOCK		5. TYPE OF REPORT & PERIOD COVERED Progress, April 1984 6. PERFORMING ORG. REPORT NUMBER
7. AUTHOR(s) ROBERT L. TOKAR and DONALD A. GURNETT		8. CONTRACT OR GRANT NUMBER(s) N00014-76-C-0016,
9. PERFORMING ORGANIZATION NAME AND ADDRESS Department of Physics and Astronomy The University of Iowa Iowa City, IA 52242		10. PROGRAM ELEMENT, PROJECT, TASK AREA & WORK UNIT NUMBERS
11. CONTROLLING OFFICE NAME AND ADDRESS Electronics Program Office Office of Naval Research Arlington, VA 22217		12. REPORT DATE April 1984 13. NUMBER OF PAGES 48
14. MONITORING AGENCY NAME & ADDRESS(if different from Controlling Office)		15. SECURITY CLASS. (of this report) UNCLASSIFIED 15a. DECLASSIFICATION/DOWNGRADING SCHEDULE

16. DISTRIBUTION STATEMENT (of this Report)

Approved for public release; distribution is unlimited.

17. DISTRIBUTION STATEMENT (of the abstract entered in Block 20, if different from Report)

18. SUPPLEMENTARY NOTES

To be published in J. Geophys. Res.

19. KEY WORDS (Continue on reverse side if necessary and identify by block number)

Bow shock
Whistler mode noise

20. ABSTRACT (Continue on reverse side if necessary and identify by block number)

(See following page)

DD FORM 1 JAN 73 1473 EDITION OF 1 NOV 65 IS OBSOLETE
S/N 0102-LF-014-6601

UNCLASSIFIED

SECURITY CLASSIFICATION OF THIS PAGE (When Data Entered)

DTIC COPY INSPECTED

ABSTRACT

In this study, the propagation and growth of whistler mode waves generated by electron beams within Earth's bow shock is investigated using a planar model for the bow shock and a model electron distribution function. Within the shock, the model electron distribution function possesses a field-aligned $T_\perp > T_\parallel$ beam that is directed toward the magnetosheath. Waves with frequencies between about 1 and 100 Hz with a wide range of wave normal angles are generated by the beam via Landau and anomalous cyclotron resonances. However, because the growth rate is small and because the wave packets traverse the shock quickly, these waves do not attain large amplitudes. Waves with frequencies between about 30 and 150 Hz with a wide range of wave normal angles are generated by the beam via the normal cyclotron resonance. The ray paths for most of these waves are directed toward the solar wind although some wave packets, due to plasma convection, travel transverse to the shock normal. These wave packets grow to large amplitudes because they spend a long time in the growth region. The results suggest that whistler mode noise within the shock should increase in amplitude with increasing upstream θ_{Bn}. The study provides an explanation for the origin of much of the whistler mode turbulence observed at the bow shock.

I. INTRODUCTION

The discovery of field-aligned electron beams within the Earth's bow shock by the ISEE-2 fast plasma experiment [Feldman et al., 1982] is an important contribution to existing measurements of electron distribution functions at collisionless shocks. Two important features of the beams are that they are moving toward the magnetosheath and that the beam energy, which ranges up to about 100 eV, increases with increasing distance from the solar wind boundary of the shock. Although the observed characteristics of the electron beams have not yet been categorized with respect to upstream solar wind parameters, it is known that the beams are observed for both quasi-parallel and quasi-perpendicular bow shock geometries. It is thought that the beams are produced by a macroscopic electric field within the shock. To obtain a qualitative understanding of how this electric field may be created, the reader can consult the paper by Wu [1982].

It is natural that the discovery of field-aligned electron beams at the bow shock would initiate studies on instabilities generated by the beams. The interest in plasma instabilities stems from the fact that many types of plasma waves are often observed at the bow shock (e.g., Fredricks et al. [1968] and Rodriguez and Gurnett [1975]). In addition, plasma turbulence is thought to play an important dissipative role at the shock. Since the discovery of the beams, two studies have investigated the linear Vlasov stability of the observed electron

distributions. In Thomsen et al. [1983] it is shown that the electron beams generate electrostatic waves via Landau resonance while in Tokar et al. [1984] it is shown that the beams can also generate whistler mode waves via Landau and cyclotron resonance. Because this study is an extension of the work reported in Tokar et al. [1984], it is desirable to briefly discuss the main results of that paper.

Figure 1, reproduced from Tokar et al. [1984], illustrates typical observations of whistler mode waves at the bow shock. In the top panel observations of the wave magnetic fields, measured by the ISEE 1 plasma wave experiment on December 13, 1977, are shown in ten frequency channels covering the range 5.6 Hz to 1 kHz. The bottom panel depicts the magnetic field magnitude measured by the magnetic field experiment on ISEE 1. The magnetic ramp defining the shock transition region is clearly visible, with the upstream boundary at about 17:35:05.0. Within the magnetic ramp, whistler mode noise can be seen in the bottom six frequency channels of the wave magnetic field data. The noise is most intense within the shock and extends into the upstream solar wind and downstream magnetosheath.

To investigate the possibility that the field-aligned electron beams present in the shock generate the whistler mode noise, Tokar et al. [1984] analyzed the linear Vlasov stability of three analytic fits to electron velocity distribution data obtained by the fast plasma experiment within the shock. The analysis shows that the three electron distribution functions are unstable to whistler mode waves. In all cases, the free energy regions in the distribution function that

are responsible for the wave growth are attributable to the field-aligned beam. Waves are generated by Landau and cyclotron resonance and have wave vectors directed toward both the magnetosheath and the solar wind. The unstable waves have plasma rest frame frequencies between about 1 and 100 Hz and wave normal angles that range from 0° to the resonance cone angle. In addition, the growth rates for many of the waves appeared to be large enough to give rise to the large amplitude whistler mode noise shown in Figure 1.

This study extends the analysis given in Tokar et al. [1984] and has two primary purposes. The first is to investigate the generation of whistler mode waves throughout the shock transition region, and the second is to investigate the propagation and path integrated amplification of the waves. The previous study treated only three positions within the shock. In this study, a simple model electron distribution function is constructed that is a function of position within the shock transition region. The distribution evolves from an isotropic Maxwellian at the solar wind to an isotropic modified Lorentzian at the magnetosheath and generates a broad spectrum of whistler mode waves. Using a simple model for the shock, ray paths for the generated whistler mode waves are calculated. The path integrated amplification along the ray path is obtained using the model electron distribution function and a linear growth rate formula.

II. MODEL BOW SHOCK AND ELECTRON DISTRIBUTION FUNCTION

In this section the simple models for the bow shock region and the electron distribution function are presented. These models provide the description of the geometry and plasma parameters within the shock that is needed to investigate the generation and propagation of the whistler mode waves.

A. Planar Bow Shock Model

For simplicity, a planar model is adopted to describe the bow shock region. The planar assumption is justified because the length scales along the shock normal and transverse to the shock normal are both much less than the radius of curvature of the shock. Figure 2 illustrates the coordinate system and overall geometry of the model. The $\hat{z}$ axis is along the shock normal with positive $\hat{z}$ directed from the solar wind to the magnetosheath. The shock transition region extends for 100 km in the $\hat{z}$ direction and separates the upstream solar wind from the downstream magnetosheath. The chosen thickness of the shock, 100 km, is in good agreement with the measurements of Russell et al. [1979].

In order to calculate ray paths for whistler mode waves using the planar bow shock model, the electron concentration, magnetic field vector, and plasma flow vector must be known throughout the shock transition region. In the planar model, these quantities are a

function only of z, the penetration into the shock. They are assumed to vary as follows:

1) The electron concentration, n, and magnetic field magnitude, B, increase linearly within the shock transition region from upstream solar wind values to downstream magnetosheath values. The increase in n across the shock is from 2.5 cm^{-3} to 10 cm^{-3} while the increase in B across the shock is from 5 gammas to 20 gammas. These values correspond to the values measured during the December 13, 1977, shock crossing analyzed in Tokar et al. [1984].

2) The direction of the magnetic field follows from the assumed increase in the magnitude of $\vec{B}$ and the condition that the component of $\vec{B}$ in the direction of the shock normal, $\hat{n}$, remain constant throughout the shock transition region. Figure 2 illustrates a magnetic field line for the case when the upstream angle between $\vec{B}$ and $\hat{n}$, θ_{Bn}, is 45°. Two values of θ_{Bn} are treated, 45° and 65°.

3) The plasma flow velocity, $\vec{v}_f$, is taken to be in the $\hat{z}$ direction throughout the shock transition region. The magnitude of $\vec{v}_f$ decreases with increasing z such that the normal component of the number flux, $n|\vec{v}_f|$, remains constant throughout the transition region. In the model adopted, the plasma flow speed decreases from 400 km/s at the solar wind to 100 km/s at the magnetosheath.

In summary, within the shock transition region the electron concentration and magnetic field magnitude increase linearly, the normal

component of $\vec{B}$ is constant, the plasma flow velocity is in the $\hat{z}$ direction, and the normal component of the number flux is constant.

It should be noted that the adopted increases in the electron concentration and magnetic field magnitude across the shock, intended to agree with observation, do not satisfy MHD jump conditions for shocks. A model based on the MHD jump conditions can be constructed, for example, by reducing the jump in the electron concentration until a desired jump in the magnetic field magnitude is obtained. The calculated upstream and downstream parameters must then be connected in some fashion across the shock. The differences in the adopted model and a model constructed using the MHD jump conditions do not significantly effect the primary results of this study. In particular, the neglect of a transverse plasma flow within the shock does not significantly affect the integrated growth calculations because the wave packets that grow to large amplitudes have $\vec{v}_g$ primarily in the transverse direction and $|\vec{v}_g| > |\vec{v}_f|$.

It is also evident that familiar features at supercritical shocks, such as overshoots in $|\vec{B}|$ and ρ and a magnetic "foot", are not included in the model adopted. Such features can affect both the calculated ray paths and growth rates. However, it is difficult to construct a model electron distribution function throughout the shock that reflects these structures. For this reason, the simple planar model with linearly increasing $|\vec{B}|$ and n is adopted to obtain a semi-quantitative picture of the propagation of the whistler mode waves.

B. Model Electron Distribution Function

It is desirable to obtain a model electron distribution function that is a function of position within the shock transition region so that the generation, propagation, and growth (or damping) of whistler mode waves throughout the transition region can be studied in detail. In this study, a simple model electron distribution function is constructed such that its features are consistent with experimental results. An alternative approach would be to solve the Vlasov-Maxwell equations throughout the shock. While such a solution would possess a self-consistency absent in the simple model adopted, obtaining an accurate solution would be a difficult task. Consequently, the program adopted is to construct a simple model that agrees with experimental findings.

The analytic function that often provides a good fit to the electron distribution functions measured in the shock is the sum of a modified Lorentzian and a convected Maxwellian [Feldman et al., 1983]. Specifically, the electron distribution function data in the plasma rest frame is fit to a function of the form

$$F(v_\perp, v_\parallel) = F_1 + F_2 \tag{1}$$

where

$$F_1 = \frac{C_1}{\left(1 + \left(\frac{v_\parallel^2 + v_\perp^2}{v_1^2}\right)^R\right)^{P/R}} \tag{2}$$

is the modified Lorentzian and

$$F_2 = C_2 \exp\left(\frac{-m(v_\parallel - v_2)^2}{2kT_\parallel}\right) \exp\left(\frac{-mv_\perp^2}{2kT_\perp}\right) \qquad (3)$$

is the convected Maxwellian. In these equations, $v_\perp$ and $v_\parallel$ are the electron speeds perpendicular and parallel to the magnetic field, respectively, $T_\perp$ and $T_\parallel$ are the perpendicular and parallel temperatures of the beam, respectively, v_1 is the breakpoint speed of the modified Lorentzian, v_2 is the convection speed of the beam, m is the electron mass, k is Boltzmann's constant, and C_1, C_2, R and P are constants.

Referring to Equations 2 and 3 it can be seen that the following eight parameters must be known throughout the shock: C_1, C_2, v_1, v_2, $T_\parallel$, $T_\perp$, P and R. To construct functions that describe the variation of these parameters with position in the shock transition region the following experimental results are employed.

1) As the transition region is traversed by the spacecraft, the electron distribution function evolves smoothly from the upstream solar wind distribution to the downstream magnetosheath distribution. A typical solar wind electron distribution function is an isotropic Maxwellian with a temperature of about 1.5×10^5°K. A typical magnetosheath electron distribution function is a modified Lorentzian with $R \approx 4.0$, $P = R-1$ and $v_1 \approx 6 \times 10^8$ cm/s [Feldman et al., 1983].

2) The electron distribution function in the shock transition region has both a beam component and a flat-topped component. The convection speed of the beam, v_2, increases with increasing shock penetration. The increase is consistent with the interpretation that the incoming solar wind electrons are accelerated by a macroscopic electric field within the shock transition region. The breakpoint speed of the flat-topped component of the distribution is approximately equal to the beam convection speed (i.e., $v_1 \approx v_2$) [Feldman et al., 1983].

3) The perpendicular temperature of the beam, $T_\perp$, is accurately modeled by assuming that the first adiabatic invariant of the electrons is conserved as the electrons move from the solar wind to the magnetosheath. The parallel temperature of the beam, $T_\parallel$, decreases with increasing shock penetration. The decrease in $T_\parallel$ is qualitatively explained by the fact that the electrons are being accelerated along $\vec{B}$. A value of $T_\parallel$ equal to about 2×10^{4}°K is typical near the center of the shock transition region [Feldman et al., 1983].

Consistent with the above points, the following simple models are chosen to describe the evolution of the electron distribution function within the shock transition region.

In agreement with point 1 above, the distribution evolves from an isotropic Maxwellian with a temperature of 1.5×10^{5}°K at the solar wind (z = 0 km) to an isotropic modified Lorentzian with $v_1 = 6 \times 10^{8}$ cm/s and R = 4, P = R - 1 at the magnetosheath (z = 100 km). This

evolution is accomplished through the coefficients C_1 and C_2 in Equations 2 and 3. The coefficient C_1 in Equation 2 increases linearly from the value 0. at the solar wind to 1. at the magnetosheath while C_2 in Equation 3 decreases linearly from the value 1. at the solar wind to 0. at the magnetosheath. An additional constant multiplies the entire electron distribution function to ensure that the integral of $F(v_\perp, v_\parallel)$ over all velocity space is equal to the assumed electron concentration. This constant is a function of z because, in the planar bow shock model, the electron concentration is a function of z. It can be verified that at about z = 30 km half of the particles reside in the convected Maxwellian and half reside in the modified Lorentzian.

In agreement with point 2 above, v_1 is set equal to v_2. The convection speed of the beam, v_2, ranges from 0 cm/s at z = 0 km to about 6×10^8 cm/s at z = 100 km. As a function of z, the convection speed increases as would the speed of an electron that is being accelerated by a constant electric field of magnitude 1 volt/km. This corresponds to a potential drop across the shock of 100 volts and results in beam energies within the shock transition region that are in good agreement with the measurements of Feldman et al. [1983].

In agreement with point 3 above, the perpendicular temperature of the beam is calculated assuming that the first adiabatic invariant of the electrons is conserved throughout the transition region. The parallel temperature of the beam decreases linearly from 1.5×10^{5}°K at z = 0 km to 2×10^{4}°K at z = 50 km. For z greater than 50 km, $T_\parallel$ is equal to 2×10^{4}°K.

The above discussion defines the electron distribution function throughout the shock transition region. Contour plots of the base 10 logarithm of the model distribution, spanning one order of magnitude of $F(v_\perp, v_\parallel)$, are shown in Figure 3 for six positions within the shock transition region. This figure illustrates that the distribution function evolves from a relatively cool Maxwellian at the solar wind (z = 0 km) to a hotter modified Lorentzian at the magnetosheath (z = 100 km). With increasing z, the convection speed and ratio $T_\perp/T_\parallel$ for the beam increase.

III. WHISTLER MODE STABILITY OF THE MODEL DISTRIBUTION

Combining the model electron distribution function described in the previous section with an expression for the linear growth rate of whistler mode waves, the growth of whistler mode waves throughout the shock transition region can be investigated. The equation used to calculate the growth rate is identical to the equation given in Kennel and Wong [1967] and Tokar et al. [1984]. Because a detailed discussion of the whistler mode instability mechanisms for electron distributon functions measured in the shock transition region is given in Tokar et al. [1984], only a brief discussion will be given here. The primary purpose of this section is to summarize the unstable wave frequencies for the model electron distribution function.

For the model electron distribution function described in the previous section, the unstable whistler mode waves frequencies and wave normal angles are a function of penetration into the transition region, z. This is because the evolution with z of the velocity distribution causes the conditions for instability to be functions of z. Before presenting the unstable frequencies for the model distribution, a brief discussion of how the evolution of the model distribution with z affects the conditions for instability is desirable.

In Tokar et al. [1984] it is shown that for generation via the normal and anomalous cyclotron resonances the distribution must possess regions of sufficiently large anisotropy at the cyclotron resonance

velocities. In the model distribution this anisotropy is due to the increase in the beam temperature ratio, $T_\perp/T_\parallel$, with increasing z. Because the cyclotron resonance velocities must remain in regions of large anisotropy and because the beam energy increases with z, as illustrated in Figure 3, it is expected that the unstable frequencies will be functions of z. In Tokar et al. [1984] it is also shown that for growth via the Landau resonance, the distribution must possess a positive and sufficiently large $\frac{k_\parallel}{|k_\parallel|} \frac{\partial F}{\partial v_\parallel}$ at the wave phase velocity. From an inspection of Figure 3 it is clear that as the Maxwellian component of the model distribution evolves away from the $v_\parallel = 0$ axis, this condition will be satisfied for $k_\parallel < 0$ if z is less than about 50 km. As z increases from 50 km to 100 km, the parallel derivative of $F(v_\perp, v_\parallel)$ decreases to zero because the dominant component of the distribution is the isotropic modified Lorentzian.

Figures 4 and 5 summarize the unstable plasma rest frame frequencies for the model electron distribution function described in the previous section. It should be noted that the unstable frequencies are shown only as a function of position within the shock. The unstable wave normal angles for a given frequency are not summarized. This is because the results obtained in Tokar et al. [1984] apply to the model electron distribution function with the main point being that for a given frequency an appreciable range of wave normal angles is usually unstable.

In Figure 4 the unstable frequencies for generation via the normal cyclotron resonance are shown as a function of z. This resonance is the $m = -1$ contribution to the growth rate expression employed by Tokar et al. [1984]. For this generation mechanism, the waves all have $k_{\parallel} > 0$, corresponding to wave vectors directed toward the solar wind. The spectrum of unstable frequencies is in good agreement with the range obtained for the three electron distributions analyzed in Tokar et al. [1984]. The increase in the magnitudes of the unstable frequencies with increasing z locates the normal cyclotron resonance velocity in the region of large anisotropy associated with the field-aligned beam. The distribution is stable for small values of z because the beam temperature ratio, $T_{\perp}/T_{\parallel}$, is small. Near the center of the shock transition region the cyclotron resonant interactions are strongest. This is because in this region $T_{\perp}/T_{\parallel}$ is large and the Maxwellian component of the model distribution is appreciable.

In Figure 5 the unstable frequencies for generation via the Landau and anomalous cyclotron resonances are shown as a function of z. These resonances are the $m = 0$ and $+1$ contributions to the growth rate expression employed by Tokar et al. [1984]. For these generation mechanisms, the waves all have $k_{\parallel} < 0$, corresponding to wave vectors directed toward the magnetosheath. In agreement with expectations, the distribution is stable for values of z greater than about 50 km. The range of unstable frequencies is in good agreement with the range obtained for the distributions analyzed in Tokar et al. [1984].

IV. RAY PATHS AND INTEGRATED AMPLIFICATION

In the last section, the unstable whistler mode frequencies are summarized for the model electron distribution function as a function of position within the shock transition region. In this section the subsequent propagation and growth (or damping) of the generated whistler mode waves are discussed.

Figures 4 and 5 show that within the shock transition region the growth rate for a given whistler mode wave frequency is positive in only a limited region. The positions within the shock where the growth rate is positive act as *amplification regions* for whistler mode wave packets. To compute the overall amplification we assume that a background of very weak whistler mode noise with a wide range of wave normal angles is available for amplification from the solar wind. Neubauer et al. [1977] have reported that a background continuum of whistler mode noise is a nearly ubiquitous feature of the solar wind.

In this study the ray paths emanating from the source location are calculated using the planar bow shock model and the WKB approximation (i.e., the geometrical optics limit). The amplification along the ray path is calculated using the model electron distribution function and the linear growth rate expression given in Kennel and Wong [1967] and employed in Tokar et al. [1984]. Although the validity of this procedure in the turbulent shock transition region may be questionable at

low frequencies where the wavelength becomes comparable to the thickness of the transition region, the results provide at least a qualitative understanding of the subsequent propagation of the generated waves.

A first-order validity criterion for ray tracing in the transition region is that the characteristic scale length for changes in the plasma parameters must be larger than the wavelength of the waves investigated. A more quantitative validity criterion for a magnetized plasma is difficult to derive [Budden, 1961]. Because the characteristic scale length is the thickness of the transition region, 100 km, in this study the ray tracing calculations are limited to waves with wavelengths less than about 25 km. This condition eliminates consideration of the low frequency (1-20 Hz) waves generated by the Landau and anomalous cyclotron resonances. However, this restriction is not serious because the results indicate that only the waves generated by the normal cyclotron resonance are amplified to significant levels above the background noise.

To facilitate the understanding of the ray tracing procedure, the steps followed in a typical calculation will be listed individually. Before proceeding, it should be noted that the procedure is complicated somewhat by the fact that the plasma flow speed is a function of the position coordinate within the shock, z. The situation is analogous to the refraction of sound waves produced by a gradient of the wind velocity (e.g., see Landau and Lifshitz [1959]). Although this effect is included in the calculations, the change in the wave normal angle along the ray path due to the gradient in the plasma flow speed is small

compared to the changes produced by the gradients in the electron concentration and magnetic field magnitude.

The steps followed in the ray tracing procedure are given below.

1) For a chosen position within the shock transition region, z, a real wave frequency, ω_r, and initial wave normal angle, θ_o, are selected for which the growth rate, $\omega_i(z)$, is positive. In this study the initial wave normal angles 0° and 45° are analyzed. For the initial wave normal angle of 0°, the direction of the wave vector is along the magnetic field. However, for the initial wave normal angle of 45°, the possible wave vectors lie on a cone with axis the magnetic field direction and half angle equal to 45°. Of this set of initial wave vector orientations the two wave vectors that lie in the plane of the planar bow shock model are investigated.

2) The magnitude of the wave vector, $|\vec{k}|$, and the group velocity of the wave packet, $\vec{v}_g$, are calculated using the wave normal angle and the cold plasma whistler mode dispersion relation. For the frequencies of interest in this study, a good approximation for the dispersion relation is [Stix, 1964]

$$\left(\frac{ck}{\omega_r}\right)^2 = \frac{\omega_p^2}{\omega_r(\omega_g \cos\ \theta - \omega_r)} \quad . \qquad (4)$$

In this equation, ω_p is the electron plasma frequency, ω_g is the electron gyrofrequency, and c is the speed of light. The values of ω_p and ω_g at position z are calculated using the magnetic field magnitude and electron concentration models adopted for the planar shock model.

3) To obtain the ray path in the frame of reference of the planar bow shock model, the wave packet is then advanced along the vector $\vec{v}_g + \vec{v}_f(z)$ for a fixed increment of z, Δz. The vector $\vec{v}_f(z)$ is the plasma flow vector at the position z in the planar bow shock model.

4) The amplification along the segment of the ray path connecting z and $z + \Delta z$ is then calculated. Denoting the length of the segment by Δs, the amplification along the segment, $\Delta\Gamma$, is approximated by

$$\Delta\Gamma(z) = \frac{\omega_i(z)\Delta s}{|\vec{v}_g(z) + \vec{v}_f(z)|} \quad . \tag{5}$$

Over this segment of the ray path, the fields are amplified by the factor $e^{\Delta\Gamma}$.

5) Next, the wave normal angle $\theta(z + \Delta z)$ is calculated at the position $z + \Delta z$. To do so, first write the Doppler relation for $\omega'(z + \Delta z)$, the wave frequency at $z + \Delta z$ in the frame of reference of the plasma parcel at z. This equation is

$$\omega'(z + \Delta z) = \omega(z) + \vec{k}(z + \Delta z)\cdot\Delta\vec{v} \qquad (6)$$

where $\Delta\vec{v} = \vec{v}_f(z + \Delta z) - \vec{v}_f(z)$ is the relative velocity of the plasma parcels located at z and $z + \Delta z$. Next, combine Equations 4 and 6 to obtain the magnitude of the wave vector at $z + \Delta z$

$$|\vec{k}(z+\Delta z)| = \frac{\omega_p}{c}\left(\frac{\omega(z) + \vec{k}(z+\Delta z)\cdot\Delta\vec{v}}{\omega_g \cos\,\theta(z+\Delta z) - \omega(z) - \vec{k}(z+\Delta z)\cdot\Delta\vec{v}}\right)^{1/2} \qquad (7)$$

In the planar bow shock model, Snell's law requires that the component of $\vec{k}$ perpendicular to the shock normal remain constant along the ray path. Because it is difficult to solve Equation 7 for $|\vec{k}(z + \Delta z)|$, in the right-hand side of Equation 7 the approximation is made that $\vec{k}(z) \approx \vec{k}(z + \Delta z)$. This approximation retains the $\vec{k}\cdot\Delta\vec{v}$ correction to the wave frequency and is accurate for small increments in z. With this approximation, Equation 7 is solved for $|\vec{k}(z + \Delta z)|$. Snell's law then yields the equation needed to calculate the new wave normal angle, $\theta(z + \Delta z)$.

6) Finally, steps 2 through 5 are repeated with the new frequency, $\omega'(z + \Delta z)$, and wave normal angle, $\theta(z + \Delta z)$. The procedure is continued until the net amplification along the ray path, Γ, which is the sum of the values of $\Delta\Gamma$ for each ray path segment, becomes negative.

Figures 6 and 7 illustrate the relative orientations of the magnetic field vector, the wave vector, the group velocity, and the plasma flow velocity within the shock transition region. Figure 6 applies to a wave packet that is generated by the normal cyclotron resonance ($m = -1$ and $k_{\parallel} > 0$) while Figure 7 applies to a wave packet that is generated by the Landau and anomalous cyclotron resonances ($m = 0, +1$ and $k_{\parallel} < 0$). The two initial wave vector orientations for the wave normal angle θ are shown. The orientations are distinguished by the angle ϕ with the $\phi = 0°$ orientation corresponding to the wave vector with the largest component in the direction of the solar wind. The $\phi = 180°$ orientation lies on the cone of half angle θ and is in the plane of the planar bow shock model. This orientation is denoted $\phi = 180°$ because it can be visualized as being 180° in azimuth on the cone from the $\phi = 0°$ orientation.

The group velocity $\vec{v}_g$, the plasma flow velocity, $\vec{v}_f$, and the angle between $\vec{v}_g$ and $\vec{B}$, ψ are also shown in Figures 7 and 8. The relative lengths of $\vec{v}_g$ and $\vec{v}_f$ shown in these figures are typical for calculations near the center of the shock transition region. Figure 6 illustrates that when $k_{\parallel}$ is positive the plasma convection causes the ray paths to be refracted transverse to the shock normal while Figure 7 illustrates that when $k_{\parallel}$ is negative the plasma convection causes the ray paths to be refracted predominantly in the direction of the magnetosheath.

The results of the ray tracing calculations are summarized in Figures 8 and 9. Figure 8 applies to the case when the upstream angle

between $\vec{B}$ and $\hat{n}$, θ_{Bn}, in the planar bow shock model is equal to 45° while Figure 9 is for θ_{Bn} equal to 65°. These two values of θ_{Bn} illustrate the important effects that occur as the shock becomes more perpendicular. Parallel or nearly parallel geometries and perpendicular or nearly perpendicular geometries are not treated in this study due to a lack of information concerning the electron distribution function for these shocks.

The magnetic field line and several ray paths within the shock transition region are shown in Figure 8. The ray paths are labelled using wave frequency, initial wave normal angle, and value of ϕ in the format ($\omega_r/2\pi$, θ_o, ϕ). A value of ϕ for $\theta = 0°$ is not applicable and so is omitted from the ray path labels. The solid portions of the ray paths correspond to regions of growth while the dashed portions correspond to regions of damping. The amplification factor, Γ, at the position of marginal stability, $\omega_i = 0$, is given at the heads of the arrows denoting the ray path directions.

The ray paths for generation via the Landau and anomalous cyclotron resonances lie near the center of the transition region in Figure 8. The frequency analyzed, $\omega_r/2\pi = 50$ Hz, has associated wavelengths always less than 25 km and serves to illustrate the important propagation characteristics for the case $k_\parallel < 0$. Two initial wave vector orientations, $\theta_o = 45°$ with $\phi = 0°$ and $\theta_o = 45°$ with $\phi = 180°$ are treated. The case $\theta_o = 0°$ is omitted from the calculations because the growth rate is always negative for $k_\parallel < 0$ and $\theta_o = 0°$ [Tokar et al., 1984].

Figure 8 shows that the ray paths for the frequency $\omega_r/2\pi = 50$ Hz are directed toward the magnetosheath. This is due to the fact that both the group velocity and the solar wind velocity are directed toward the magnetosheath, as shown in Figure 7. For generation via the Landau and anomalous cyclotron resonances, the net amplification along the ray paths is small because the waves propagate quickly through the transition region. The values of Γ given in Figure 8, 0.5 and 0.9, are typical for all wave packets with $k_\parallel < 0$.

The ray paths for generation via the normal cyclotron resonance are shown originating on the right-hand side of Figure 8. The three frequencies treated, $\omega_r/2\pi = 70$, 90, and 110 Hz, together with the three initial wave vector orientations, illustrate all of the important propagation characteristics for the case $k_\parallel > 0$. Figure 7 illustrates that in this case the ray paths are directed toward the solar wind and the amplification factors can be large. In none of the cases do the wave packets reach the solar wind.

Figure 9 illustrates the results of the ray tracing calculations when θ_{Bn} in the planar bow shock model is equal to 65°. The format of the figure is identical to that in Figure 8. The new magnetic field geometry does not significantly affect the calculations for the waves traveling toward the magnetosheath. Again, the primary result is that the background noise is not significantly amplified.

However, the new magnetic field geometry does affect the calculations for the waves generated by the normal cyclotron resonance. As is clear from an inspection of Figure 9, many of the ray paths for generation via the normal cyclotron resonance have large amplification

factors. In particular, the largest amplification occurs when the ray path is directed nearly transverse to the shock normal. These waves grow to large amplitudes because they spend a long time in the growth region. In two cases, labeled (70, 45, 180) and (110, 45, 180), the waves asymptotically approach a point where the plasma flow velocity and the $\hat{z}$ component of the group velocity are of equal magnitude and oppositely directed, in a region where the growth rate is positive. Consequently, these wave packets do not leave the growth region and grow to infinite amplitude. This infinite growth is denoted in the figure by the symbol ∞. For the same two frequencies but different source regions, the amplification factors did not return to zero within 1000 km of the source region. These ray paths are terminated at the point of marginal stability, and the values for Γ at the point of marginal stability, 13.3 and 140.7, are given.

It should be noted that if components of $\vec{B}$ and $\vec{v}_g$ out of the plane of the bow shock model are considered, the additional degree of freedom will result in additional wave packets that satisfy $\vec{v}_g \cdot \hat{z}$ equal to $-|\vec{v}_f|$. Therefore, a more accurate three-dimensional model will possess more wave packets attaining large amplitude, thereby supporting the conclusions of this study.

The results of the ray tracing calculations are summarized as follows.

1) The waves generated by the Landau and anomalous cyclotron resonances follow ray paths that are directed toward the magnetosheath. The wave packets traverse the transition region

quickly, experiencing a period of small growth followed by a period of small damping. Because these waves propagate quickly through the transition region they are not significantly amplified. Large amplitude wave packets with $k_{\parallel} < 0$ are therefore not expected to reach the magnetosheath.

2) Many of the waves generated by the normal cyclotron resonance achieve large amplitudes. The waves with largest amplitude lie in the frequency range from about 70 to 110 Hz and are generated near the center of the shock transition region, in a region where the normal component of the propagation velocity $(\vec{v}_f + \vec{v}_g)$ is small.

3) As the shock classification changes from quasi-parallel to quasi-perpendicular, the intensity of whistler mode noise at the shock increases. This is because the time a wave packet spends in the growth region increases with θ_{Bn}. This effect has been observed at the bow shock [Rodriguez and Gurnett, 1975].

V. DISCUSSION

The integrated growth calculations presented in the previous section suggest that the electron beams present in the bow shock generate whistler mode waves with large amplification factors and that the waves are absorbed within the shock transition region. At this point it is desirable to compare the predictions of the study with observations of whistler mode noise at the shock. Two comparisons can be made. The predicted frequencies of the waves can be compared with observation and the measured amplitudes of the waves can be compared with the integrated growth calculations. However, because the initial angular distributions of the observed waves are not known, the predicted wave vector directions cannot be compared with observation.

As was discussed in the last section, the instabilities generated by the normal cyclotron resonance have the largest integrated growth rates. For this reason, the unstable frequencies for generation via this resonance should be compared to the frequencies for the large amplitude noise shown in Figure 1. In Figure 1, the range in frequency over which the whistler mode noise is observed is about 5.6 Hz to 100.0 Hz. From the previous section, the predicted plasma rest frame frequencies for the large amplitude waves generated via the normal cyclotron resonance range from about 70 Hz to 110 Hz. This leads to the conclusion that the two frequency ranges are in rough agreement.

This agreement is improved if the Doppler-shift caused by the relative motion of the satellite and the plasma is taken into account. Because the wave vectors of many of the waves generated by the normal cyclotron resonance are directed into the solar wind flow, the Doppler-effect for these waves results in a measured frequency that is lower than the plasma rest frame frequency. When the wave vector has a component in the direction of the solar wind flow, the measured frequency will be higher than the plasma rest frame frequency. It is not necessary to work out the Doppler-shift for all rays because a typical calculation will illustrate the magnitude of the effect involved.

The Doppler-shifted frequency of the wave can be calculated using the equation

$$\omega = \omega' + \vec{k} \cdot \vec{v}_f \tag{8}$$

where ω is the Doppler-shifted frequency, ω' is the rest frame frequency, $\vec{k}$ is the rest frame wave vector, and $\vec{v}_f$ is the plasma flow speed. To illustrate the general effect, consider a rest frame frequency 100 Hz, the two wave vector orientations of $\theta = 45°$ with $\phi = 0°$ and $\theta = 45°$ with $\phi = 180°$, and the case $\theta_{Bn} = 45°$. From the results presented in Figure 8, these wave packets exist near $z = 50$ km and have large integrated growth rates. Employing Equation 8 to calculate the measured frequency for the two wave vector orientations, it is found that for the $\phi = 0°$ orientation the frequency is downshifted to about

91 Hz and for the $\phi = 180°$ orientation the frequency is upshifted to to about 105 Hz.

This Doppler shift can increase dramatically if highly oblique wave normal angles are considered. This is because the magnitude of the wave vector, $|\vec{k}|$, becomes large as the wave normal angle approaches the resonance cone angle, $\theta_{Res} \cong \cos^{-1}(\omega_r/\omega_g)$. However, because hot plasma effects on the whistler mode dispersion relation may be important near the resonance cone, this possibility will not be investigated in detail here.

It is also important to investigate whether or not the instabilities of this study can attain the large amplitudes of the shock associated whistler mode noise shown in Figure 1. From Neubauer et al. [1977], it is found that typical spectral densities of whistler mode noise in the solar wind near 1 AU are 10^{-3} to 10^{-2} gammas/$(Hz)^{1/2}$ for the frequency 7 Hz and 10^{-4} gammas/$(Hz)^{1/2}$ for the frequency 70 Hz. These amplitudes for the background noise are to be compared to amplitudes of whistler mode noise in the shock transition region. An estimate of the amplification required can be obtained from the ISEE-1 plasma wave receiver on December 13, 1977. Figure 1 illustrates that at 17:35:15.0 UT on this day ISEE-1 is in the shock transition region and large amplitude whistler mode noise is present. At this time, spectral densities for the noise are about 1 gamma/$(Hz)^{1/2}$ at 7 Hz and 10^{-2} gamma/$(Hz)^{1/2}$ at 70 Hz.

From these results, it is concluded that the total amplification of the background noise must be a factor of 10^2 or 10^3. This corresponds to a range in Γ from about 5 to 7. It is clear from an inspection of Figures 8 and 9 that many of the waves generated via the normal cyclotron resonance have amplification factors large enough to give rise to the large amplitude whistler mode noise at the shock. This noise is expected to have maximum intensity near the center of the shock transition region or magnetic ramp. This is in agreement with Figure 1 where the noise has maximum intensity near the center of the shock transition region at about 17:35.13.0 UT.

This study demonstrates that many of the whistler mode waves generated by electron beams in the bow shock can attain the large amplitudes typical of observations at the shock. The calculated frequencies of the waves and the observed frequencies of whistler mode noise at the shock are in rough agreement. The agreement is improved if the Doppler-shifts of oblique whistlers are taken into account. The results of the study also suggest that the amplitudes of the whistler mode noise at the shock should increase with increasing θ_{Bn}, in agreement with the observations of Rodriguez and Gurnett [1975].

The results of the study do not provide a direct explanation for the origin of the whistler mode noise in the solar wind and magnetosheath boundary regions of the shock. It is plausible that this discrepancy is a consequence of the idealized models adopted and that in actuality most of the whistler mode noise observed at the shock is generated in the transition region and propagates into the upstream solar wind and downstream magnetosheath. For example, if the wave packets depicted in Figures 8 and 9 encounter electron distributions near the solar wind or magnetosheath that are weakly or marginally stable to whistler mode waves, they will escape the transition region. This idea is consistent with a large number of plasma wave observations at shocks. In many cases, whistler mode turbulence is most intense at the shock and decreases in intensity approximately exponentially with increasing distance from the shock.

ACKNOWLEDGEMENTS

This research was supported by NASA through Grant NGL-16-001-043 with NASA Headquarters and Contract NAS5-26819 with Goddard Space Flight Center and by the Office of Naval Research through Contract N00014-76-C-0016.

PREVIOUS PAGE IS BLANK

REFERENCES

Budden, K. G., Radio Waves In the Ionosphere, Cambridge Press, 1961.

Feldman, W. C., R. C. Anderson, S. J. Bame, S. P. Gary, J. T. Gosling, D. J. McComas, M. F. Thomsen, G. Paschmann, and M. M. Hoppe, Electron velocity distributions near the Earth's bow shock, J. Geophys. Res., 88, 96, 1983.

Feldman, W. C., S. J. Bame, S. P. Gary, J. T. Gosling, D. McComas, M. F. Thomsen, G. Paschmann, N. Sckopke, M. M. Hoppe, and C. T. Russell, Electron heating within the Earth's bow shock, Phys. Rev. Lett., 49, 199, 1982.

Fredricks, R. W., C. F. Kennel, F. L. Scarf, G. M. Crook, and I. M. Green, Detection of electric-field turbulence in the Earth's bow shock, Phys. Rev. Lett., 21, 1761, 1968.

Landau, L. D., and E. M. Lifshitz, Fluid Mechanics, Pergamon Press, Section 67, pg. 259, 1959.

Neubauer, F. M., H. J. Beinroth, H. Barnstorf, and G. Dehmel, Initial results from the Helios-1 search coil magnetometer experiment, J. Geophys. Res., 42, 599, 1977.

PREVIOUS PAGE IS BLANK

Rodriguez, P., and D. A. Gurnett, Electrostatic and electromagnetic turbulence associated with the Earth's bow shock, J. Geophys. Res., 80, 19, 1975.

Stix, T. H., The Theory of Plasma Waves, McGraw-Hill, 1962.

Thomsen, M. F., H. C. Barr, S. P. Gary, W. C. Feldman, and T. E. Cole, Stability of electron distributions within the Earth's bow shock, J. Geophys. Res., 88, 3035, 1983.

Tokar, R. L., D. A. Gurnett, and W. C. Feldman, Whistler mode turbulence generated by electron beams in Earth's bow shock, J. Geophys. Res., 89, 105, 1984.

Wu, C. S., Physical mechanisms for turbulent dissipation in collisionless shock waves, Sp. Sci. Rev., 32, 83, 1982.

FIGURE CAPTIONS

Figure 1 This figure is reproduced from Tokar et al. [1984] and illustrates typical observations of whistler mode noise at the bow shock. The figure depicts data obtained with the ISEE-1 plasma wave experiment and the magnetic field experiment. The top panel shows the wave magnetic fields in ten frequency channels while the bottom panel illustrates the magnetometer data. The magnetic ramp defining the shock transition region is clearly visible as is the large amplitude whistler mode noise at the shock. The noise is most intense within the shock transition region and extends into the upstream solar wind and downstream magnetosheath.

Figure 2 This figure depicts the planar bow shock model when the upstream θ_{Bn} is equal to 45°. The shock transition region extends for 100 km in the $\hat{z}$ direction and separates the upstream solar wind from the downstream magnetosheath. The magnetic field magnitude and electron concentration are assumed to increase linearly with increasing z. Within the

shock transition region the plasma flow velocity is taken to be in the $\hat{z}$ direction and the plasma flux is constant. Due to the planar geometry, the normal component of the magnetic field is constant throughout the transition region. A magnetic field line is shown as is θ_{Bn} near the center of the transition region.

Figure 3 This figure depicts contour plots of the logarithm of the model electron velocity distribution as a function of shock penetration, z. The distribution evolves from a relatively cool Maxwellian at the solar wind (z = 0 km) to a relatively hot modified Lorentzian at the magnetosheath (z = 100 km). As the beam energy increases, the anisotropy ratio, $T_{\perp}/T_{\parallel}$, increases as does the modified Lorentzian component of the model distribution.

Figure 4 This figure summarizes the unstable frequencies as a function of shock penetration for the model distribution and generation via the normal cyclotron resonance. It is usually true that for a given frequency a wide range of wave normal angles is unstable. The increase in frequency with increasing z is due to the fact that the normal cyclotron resonance velocity must remain in regions of large anisotropy in F(z).

Figure 5 This figure summarizes the unstable frequencies as a function of shock penetration for the model distribution and generation via the Landau and anomalous cyclotron resonances. It is usually true that for a given frequency a wide range of wave normal angles is unstable. The distribution is stable for z greater than about 50 km because $\frac{k_\parallel}{|k_\parallel|} \frac{\partial F}{\partial v_\parallel}$ evaluated at the Landau resonance velocity is not sufficiently positive.

Figure 6 This figure illustrates the relative orientations of the magnetic field vector, the wave vector, the group velocity, and the plasma flow velocity for generation via the normal cyclotron resonance. All vectors lie in the plane of the figure. For a given wave normal angle, the two wave vectors that lie in the plane of the planar bow shock model are distinguished by the angle ϕ with the $\phi = 0°$ direction defined to be toward the solar wind. The $\phi = 180°$ orientation lies on the unstable cone of wave vectors and is 180° in azimuth from the $\phi = 0°$ orientation. For a given wave vector orientation, the ray path direction in the shock frame of reference is in the direction of the vector $\vec{v}_g + \vec{v}_f$. For $k_\parallel > 0$, most of the ray paths are directed toward the solar wind. However,

the $\phi = 180°$ orientation of $\vec{k}$ together with the plasma convection effect can result in a ray path directed nearly transverse to the shock normal.

Figure 7 This figure is similar to Figure 6 but illustrates the geometry for the case of generation via the Landau and anomalous cyclotron resonances. The ray path directions in the shock frame are given by the direction of the vector $\vec{v}_g + \vec{v}_f$. In all cases, the ray paths are directed toward the magnetosheath.

Figure 8 This figure illustrates the results of the propagation and integrated growth calculations when the upstream θ_{Bn} is equal to 45°. Shown are a magnetic field line and several ray paths in the shock transition region. The ray paths for generation via the Landau and anomalous cyclotron resonances originate in the lower left corner of the figure while those for generation via the normal cyclotron resonance originate on the right side of the figure. The ray paths are labeled in the format $(\omega_r/2\pi, \theta_o, \phi)$ where θ_o and ϕ specify the initial wave vector orientation. A ϕ value for $\theta_o = 0°$ is not applicable and so is omitted from the ray path labels. The solid portions of the ray paths correspond to regions of growth

while the dashed portions correspond to regions of damping. At the heads of the arrows denoting the ray path, the maximum integrated growth along the ray path is given. The ray paths terminate when the integrated growth rate becomes negative. It is evident that some of the waves generated via the normal cyclotron attain large amplitudes within the shock.

Figure 9 This figure presents the results of the propagation and integrated growth calculations when the upstream θ_{Bn} is equal to 65°. The format of the figure is similar to Figure 8. A comparison of Figure 8 and this figure suggests that the number of wave packets that attain large amplitudes within the shock increases with increasing θ_{Bn}. The largest integrated growth occurs for waves that travel transverse to the shock normal.

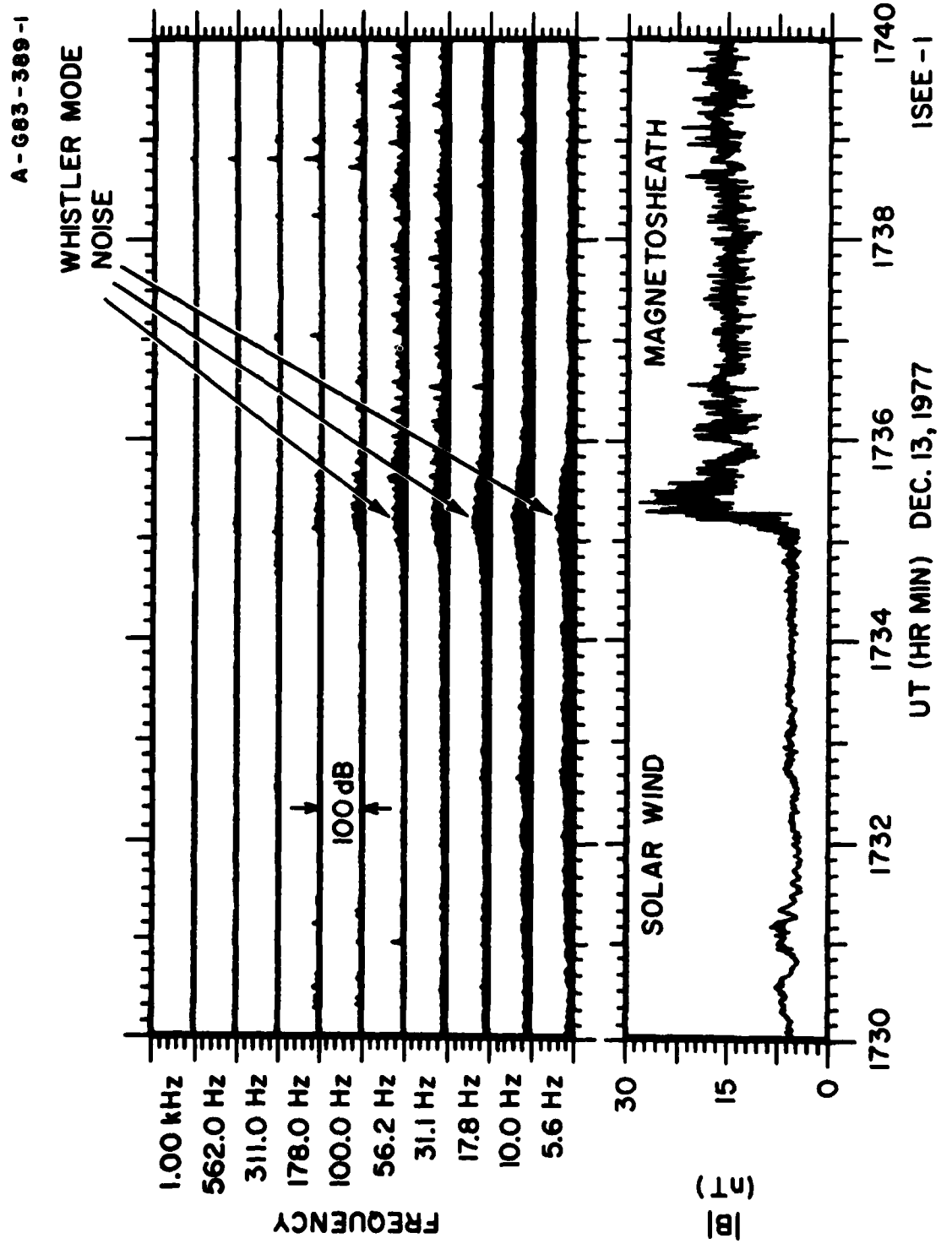

Figure 1

PREVIOUS PAGE IS BLANK

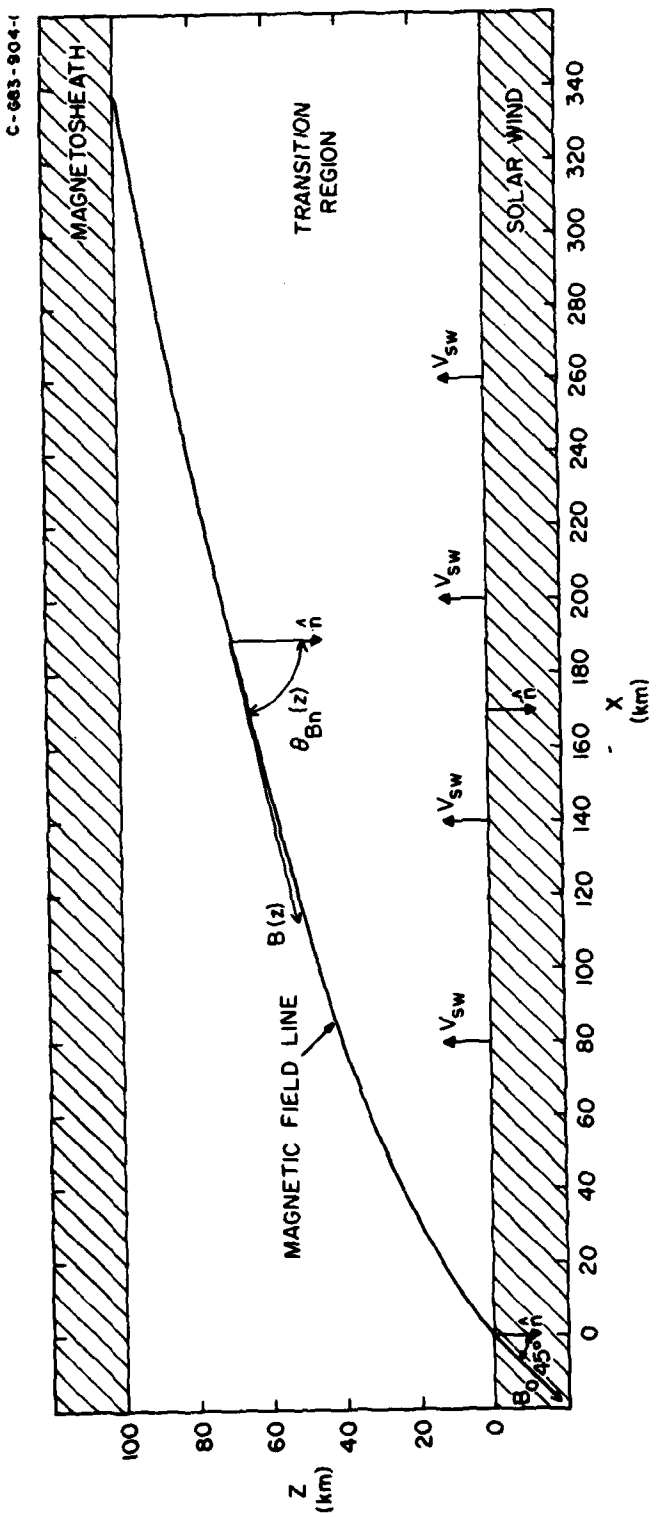
C-683-904-1
MAGNETOSHEATH
TRANSITION REGION
SOLAR WIND
MAGNETIC FIELD LINE
B(z)
$\theta_{Bn}(z)$
$\hat{n}$
V_{sw}
Z (km)
X (km)
0
20
40
60
80
100
120
140
160
180
200
220
240
260
280
300
320
340
45°

Figure 2

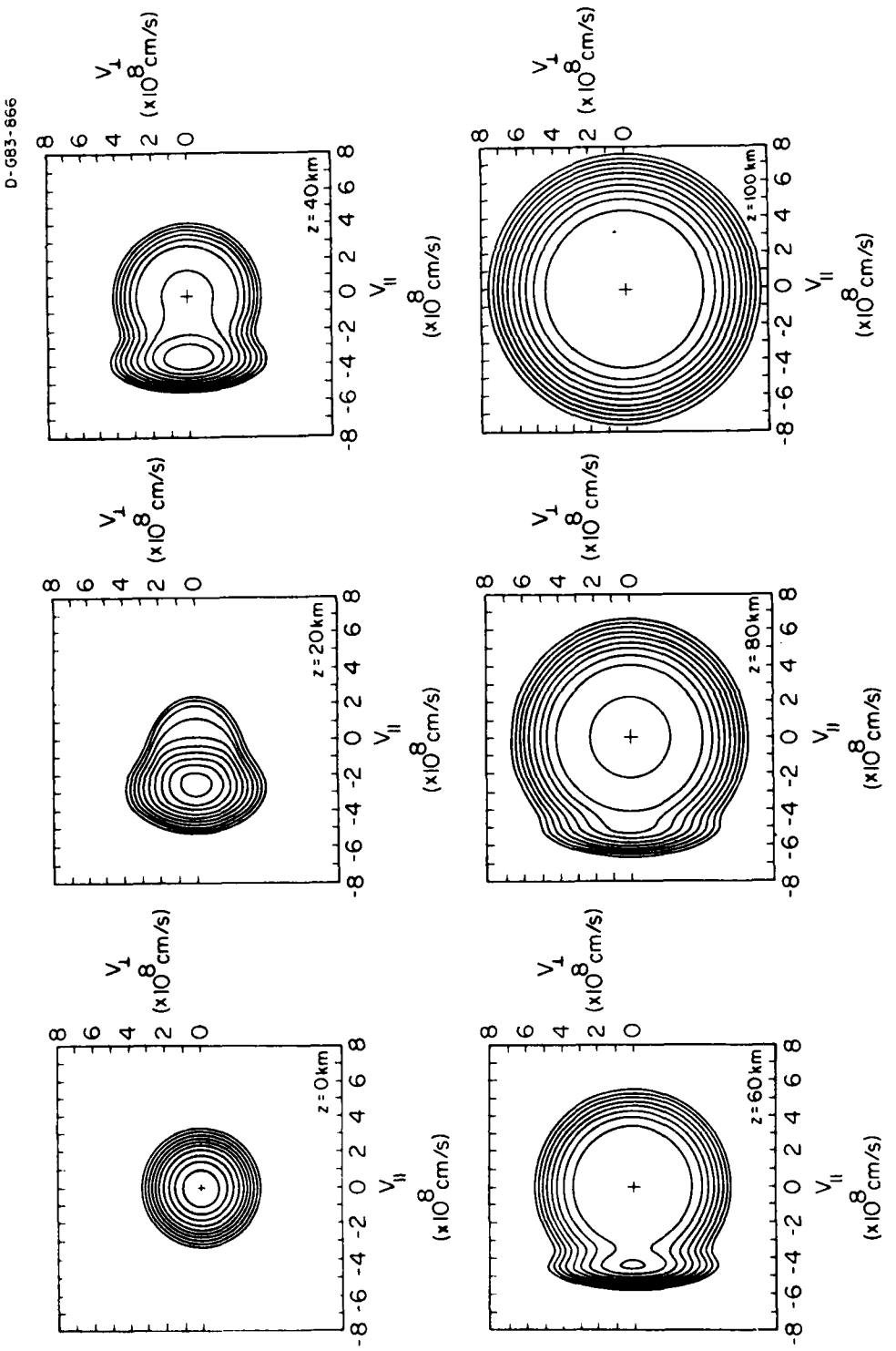
D-G83-666
z=0km
z=20km
z=40km
z=60km
z=80km
z=100km
$V_\perp$ (x10^{8}cm/s)
$V_\parallel$ (x10^{8}cm/s)

Figure 3

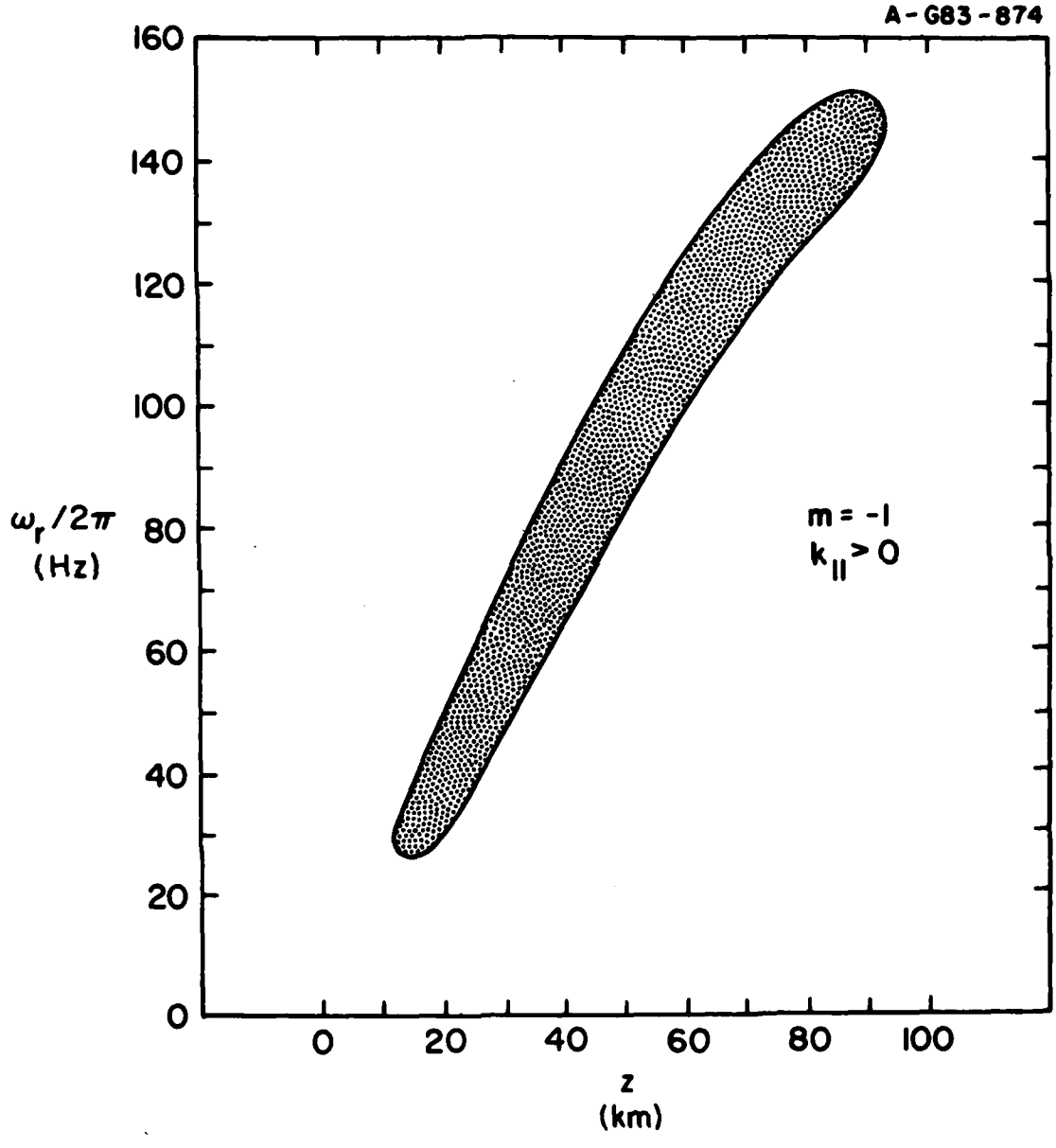
A-G83-874
160
140
120
100
80
60
40
20
0
$\omega_r/2\pi$
(Hz)
m = -1
$k_{||} > 0$
0
20
40
60
80
100
z
(km)

Figure 4

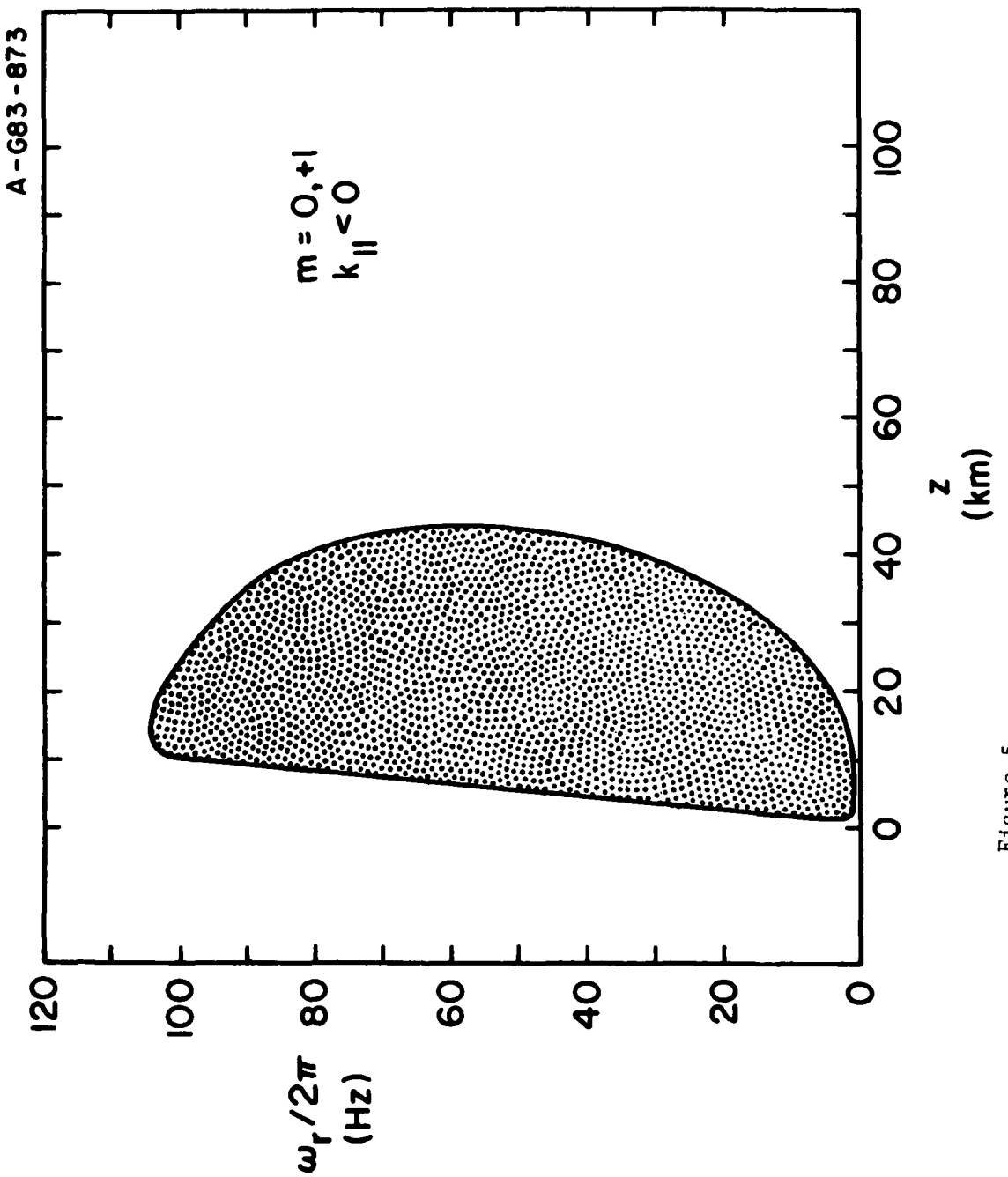

Figure 5

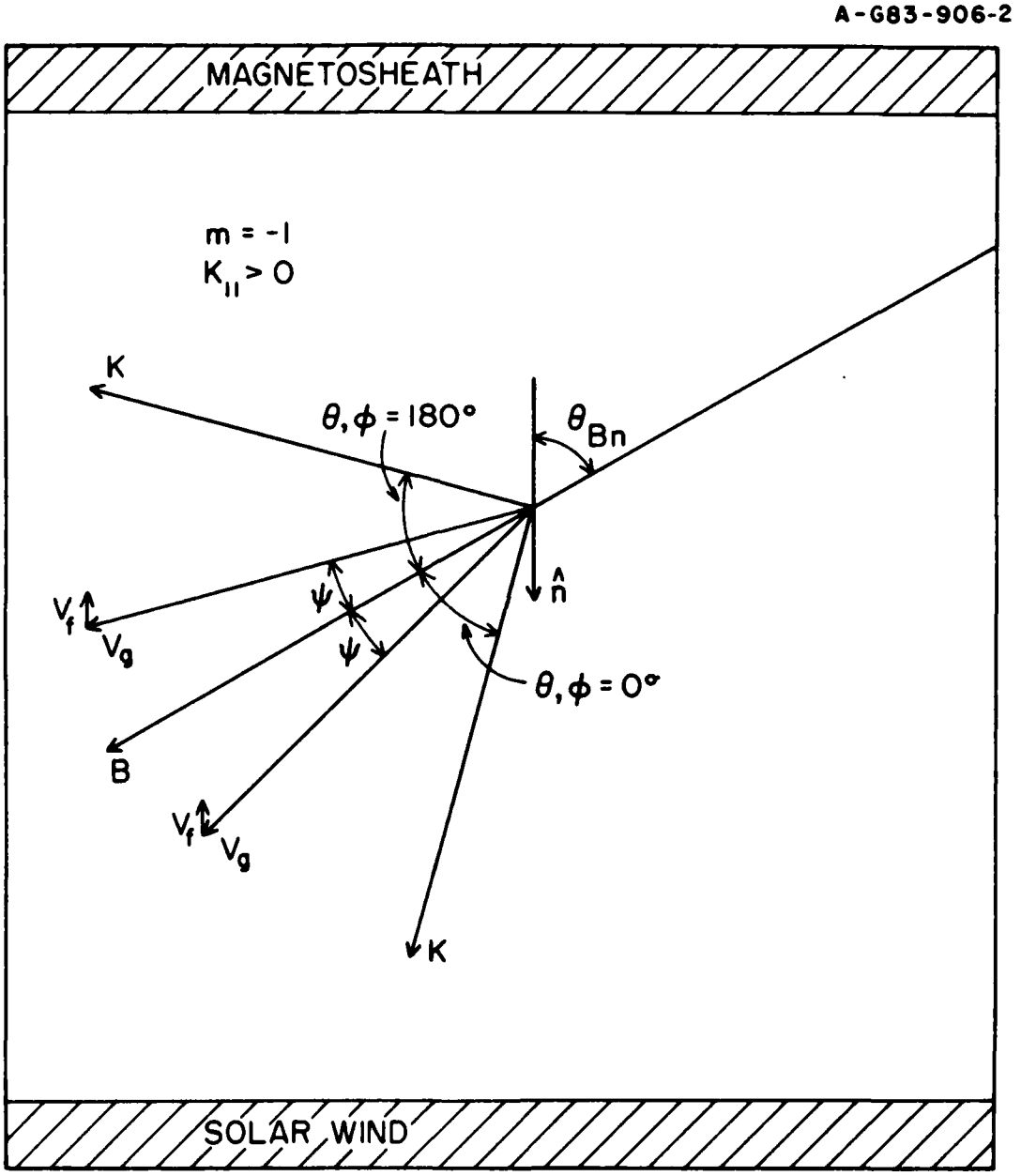
A-G83-906-2
MAGNETOSHEATH
m = -1
$K_{11} > 0$
K
$\theta, \phi = 180°$
θ_{Bn}
$\hat{n}$
V_f
V_g
ψ
ψ
$\theta, \phi = 0°$
B
V_f
V_g
K
SOLAR WIND

Figure 6

A-G83-905-2

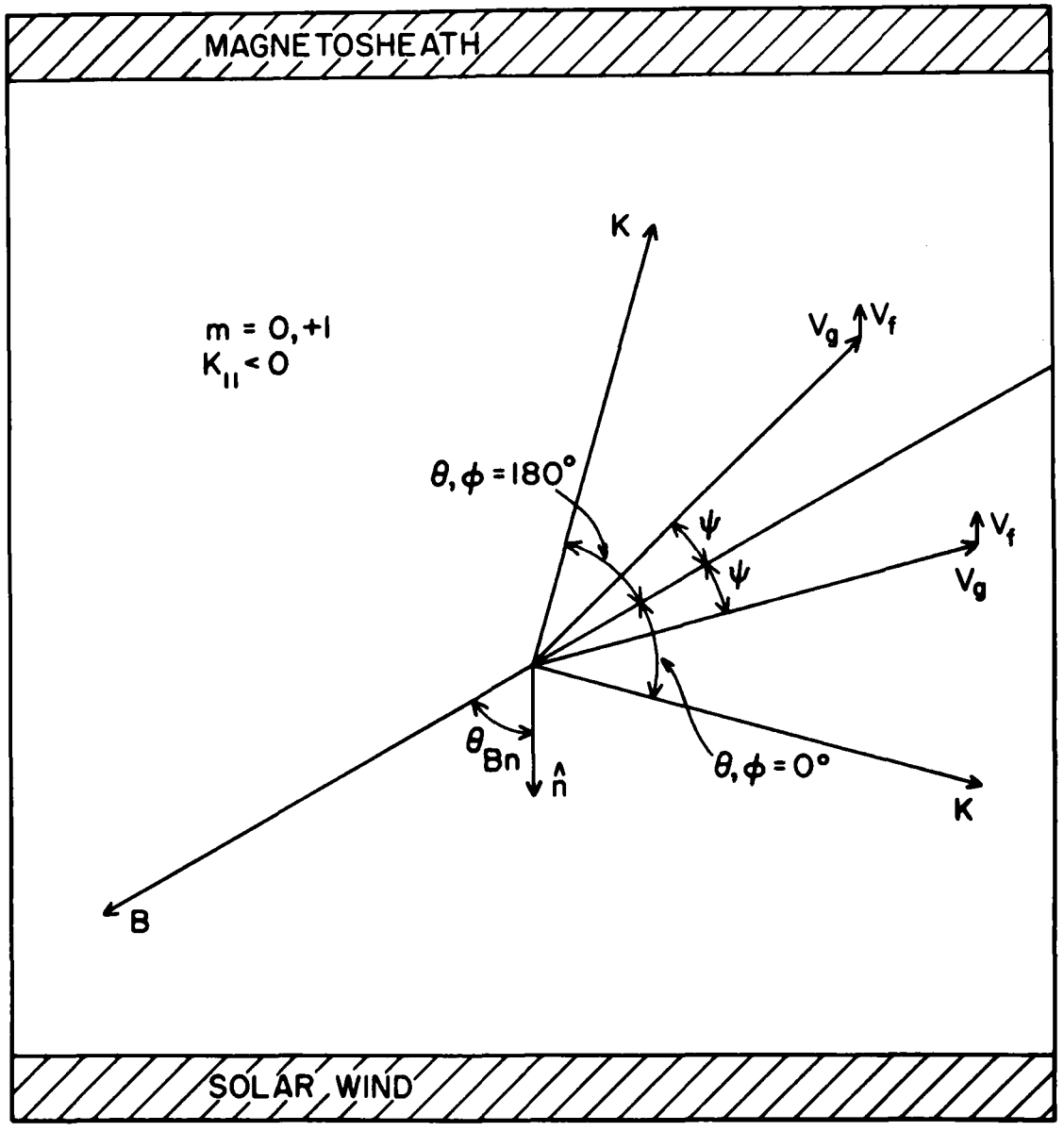

Figure 7

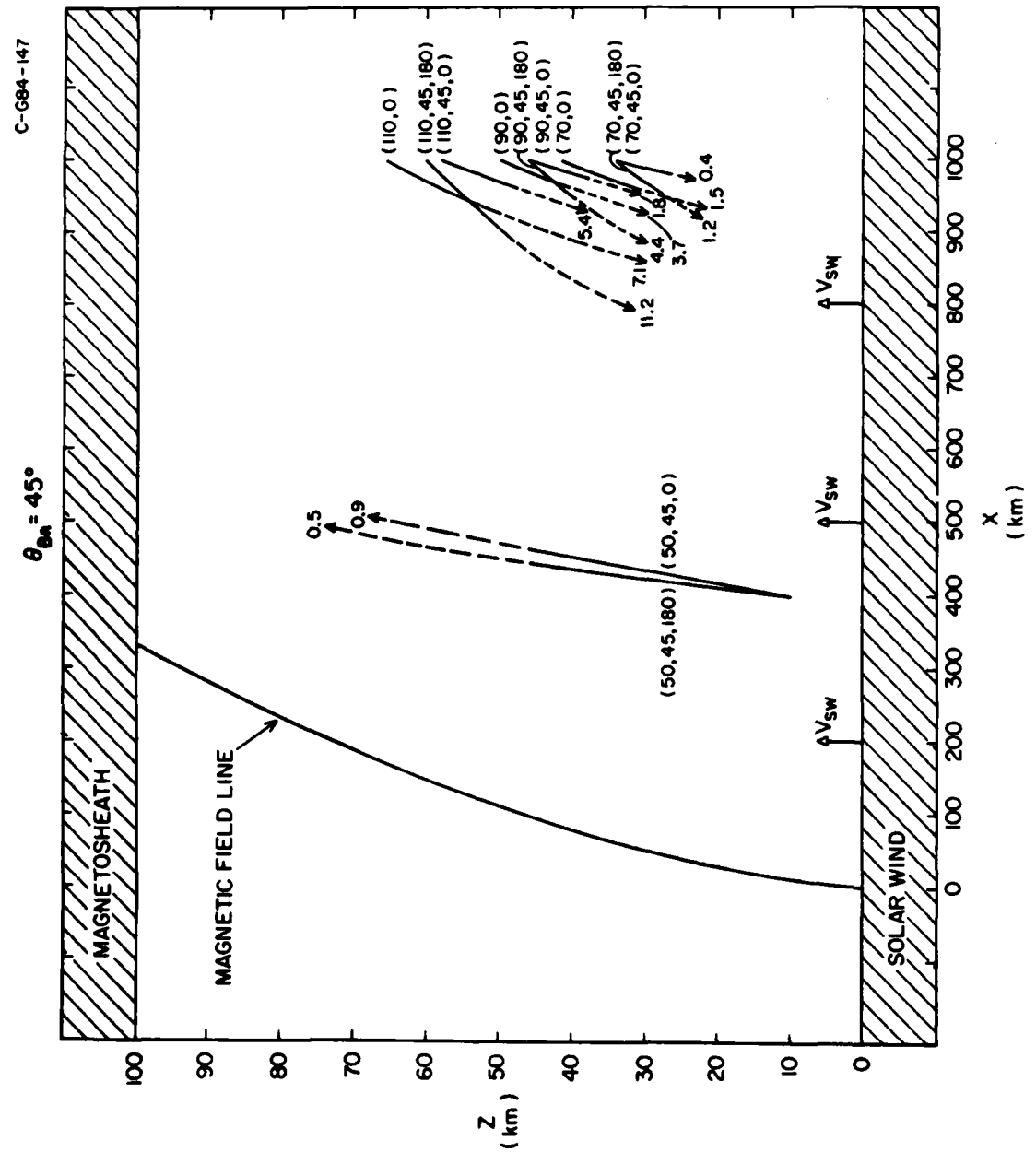
C-684-147
θ_{Bn} = 45°
MAGNETOSHEATH
MAGNETIC FIELD LINE
SOLAR WIND
(110,0)
(110,45,180)
(110,45,0)
(90,0)
(90,45,180)
(90,45,0)
(70,0)
(70,45,180)
(70,45,0)
(50,45,0)
(50,45,180)
0.5
0.9
11.2
7.1
5.4
4.4
3.7
1.8
1.5
1.2
0.4
V_{SW}
V_{SW}
V_{SW}
Z (km)
X (km)
0
10
20
30
40
50
60
70
80
90
100
0
100
200
300
400
500
600
700
800
900
1000

Figure 8

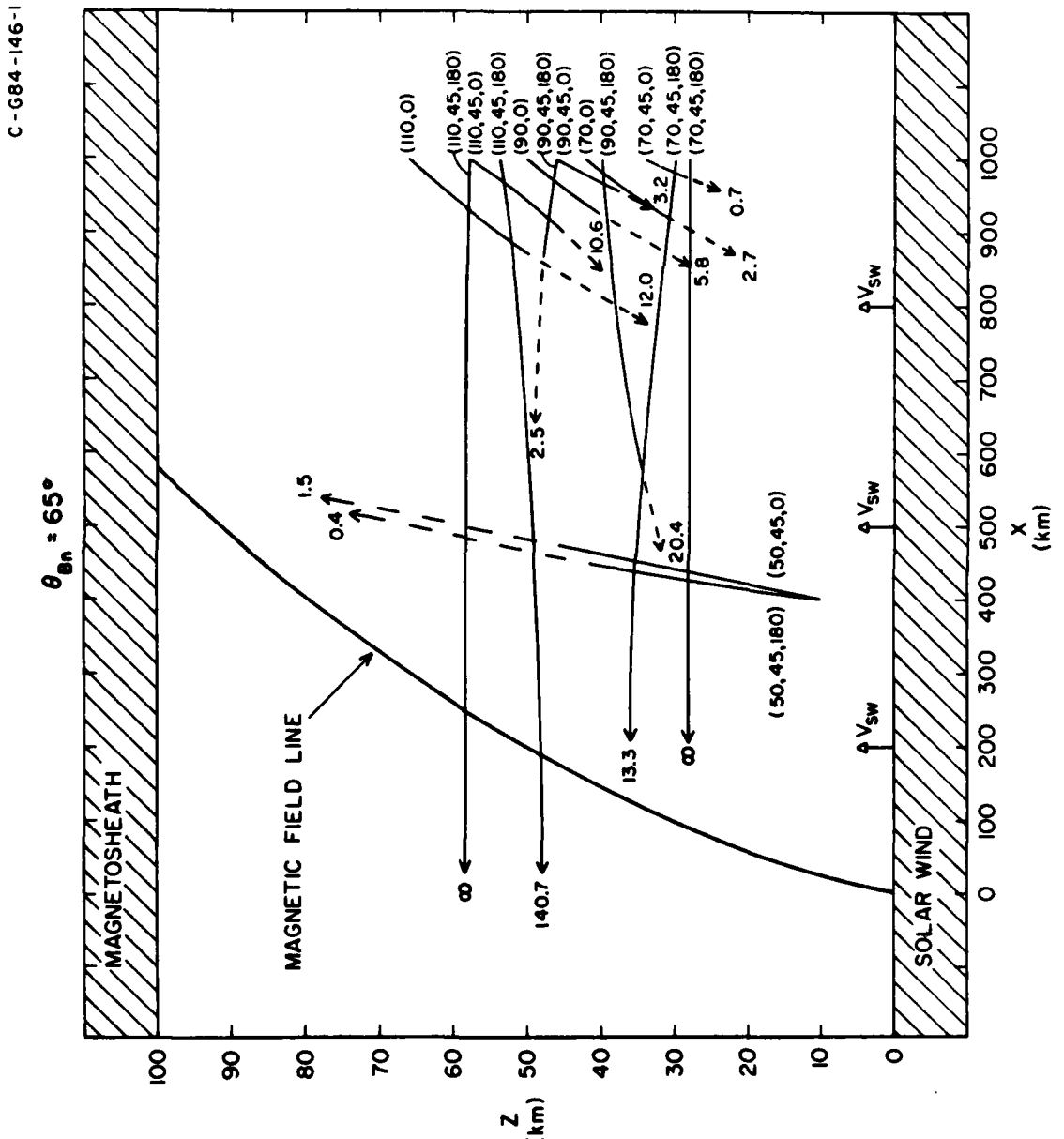
C-684-146-1
$\theta_{Bn} = 65°$
MAGNETOSHEATH
MAGNETIC FIELD LINE
SOLAR WIND
(110,0)
(110,45,180)
(110,45,0)
(110,45,180)
(90,0)
(90,45,180)
(90,45,0)
(70,0)
(90,45,180)
(70,45,0)
(70,45,180)
(70,45,180)
(50,45,0)
(50,45,180)
1.5
0.4
2.5
10.6
12.0
3.2
0.7
5.8
2.7
20.4
13.3
140.7
∞
∞
V_{SW}
V_{SW}
V_{SW}
Z (km)
X (km)
0
10
20
30
40
50
60
70
80
90
100
0
100
200
300
400
500
600
700
800
900
1000

Figure 9